Geometric Super-resolution on Push-broom Hyperspectral Imaging for Plasma Optical Emission Spectroscopy

Journal:	*Journal of Analytical Atomic Spectrometry*
Manuscript ID	JA-ART-07-2018-000235.R1
Article Type:	Paper
Date Submitted by the Author:	06-Aug-2018
Complete List of Authors:	Shi, Songyue; Texas Tech University, Department of Chemistry and Biochemistry Gong, Xiaoxia; Texas Tech University, Department of Chemistry and Biochemistry Mu, Yan; Texas Tech University, Department of Computer Science Finch, Kevin; Texas Tech University, Department of Chemistry and Biochemistry Gamez, Gerardo; Texas Tech University, Department of Chemistry and Biochemistry

Journal Name ARTICLE

Geometric Super-resolution on Push-broom Hyperspectral Imaging for Plasma Optical Emission Spectroscopy

Songyue Shi,[a] Xiaoxia Gong,[a] Yan Mu,[b] Kevin Finch[a] and Gerardo Gamez [*a]

Abstract

Push-broom hyperspectral imaging (Pb-HSI) is a powerful technique for obtaining the spectral information along with the spatial information simultaneously for various applications, from remote sensing to chemical imaging. Spatial resolution improvement is beneficial in many instances, however, typical solutions suffer from the limitation of geometric extent, lowering light throughput, or reducing the field-of-view (FOV). Sub-pixel shifting (SPS) acquires higher-resolution images, compared to typical imaging approaches, from the deconvolution of low-resolution images acquired with a higher sampling rate. Furthermore, SPS is particularly suited for Pb-HSI due to its scanning nature. In this study, an SPS approach is developed and implemented on a Pb-HSI system for plasma optical emission spectroscopy. Preliminary results showed that a periodic deconvolution error was generated in the final SPS Pb-HSI images. The periodic error was traced back to random noise present in the raw/convoluted SPS data and its frequency displays an inverse relationship to the number of sub-pixel samples acquired. Computer modelled data allows studying the effect of varying the relative standard deviation (RSD) in the raw/convoluted SPS data on the final reconstructed SPS images and optimization of noise filtering. The optimized SPS Pb-HSI technique was used to acquire the line-of-sight integrated optical emission maps

[a] Texas Tech University, Department of Chemistry and Biochemistry, Lubbock, TX, 79409-41061, USA. Email: gerardo.gamez@ttu.edu
[b] Texas Tech University, Department of Computer Science, Lubbock, TX, 79409-41061, USA.
Electronic Supplementary Information (ESI) available: See DOI: 10.1039/x0xx00000x

from an atmospheric pressure micro-capillary dielectric barrier discharge (μDBD). Selected plasma species of interest (He I, N_2, N_2^+, O) yield some insight into the underlying mechanisms. The SPS Pb-HSI technique developed here will allow implementing geometric super-resolution in many applications, for example, it will be used for extracting radially resolved information from Abel's inversion protocols, where improved fitting is expected due to the increase in resolution/data points.

Introduction

Hyperspectral imaging (HSI) allows collecting two-dimensional image scenes with spectral information at every pixel. Thus, it is widely used for obtaining spatially resolved chemical information for applications including remote sensing,[1-3] archaeology,[4] agriculture,[5] military,[6, 7] documentation,[8] forensic science,[9, 10] food analysis,[5, 11-13] and chemical imaging.[14, 15] One of the typical challenges in HSI is improving the spatial resolution. In the case where the resolution is not diffraction limited, the spatial resolution is mainly limited by the sampling rate, which in a discrete array detector, i.e. ICCD camera, is equivalent to the distance between detecting element centers and it typically defines the pixel size in conventional imaging. A usual standard solution for resolution improvement is to reduce the detecting element size. However, reducing the detecting element size will lower the geometric extent, thus lowering the light throughput. In addition, reducing the detecting element size becomes impractical after a certain point. Alternatively, image magnification is another commonly implemented solution. The drawbacks of image magnification are that the field-of-view (FOV) decreases accordingly and the numerical aperture of the optics is typically reduced. Moreover, the hardware costs may prove to be limiting.

On the other hand, sub-pixel shifting (SPS), a geometric super-resolution technique, has been developed in recent years.[16-20] In essence, it is implemented by scanning the image over the array detector by a fraction of the conventional pixel size, thus overcoming conventional limitations by using a higher sampling rate and yielding a higher resolution image. The concept of SPS is better illustrated if we assume the object to be imaged has a circular symmetry, as shown in Fig. 1a, and its diameter is equal to the pixel size. In regular imaging, the sampling distance/pixel size is set by the distance between detecting element centers. Thus, when the object's image is scanned over the pixel the detected signal intensity would correspond to that in Fig. 1c, which shows that not much about the shape of the object can be resolved, except that it can be contained within the pixel size. In contrast, the sub-pixel shifting procedure shown in Fig. 1b allows the sampling distance to be set to a fraction of the pixel width, in this case, a 1/3 of the pixel size. The detected convoluted sub-pixel shifted signal profile is shown in Fig. 1d. Then, the sub-pixel signal can be deconvoluted by subtracting the shaded area, and the resulting

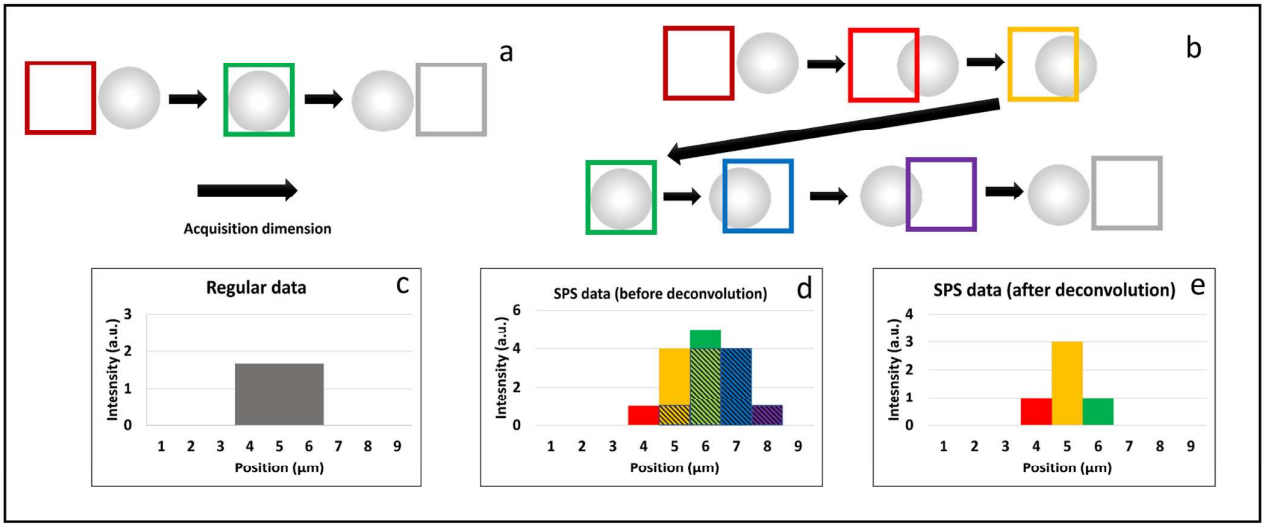

Fig. 1 Illustration of the sub-pixel shifting (SPS) concept with scanning acquisition. In regular imaging (a) sampling distance is limited by the pixel size, or box width, and leads to intensity profile (c). In contrast, SPS imaging (b) uses a smaller sampling distance compared to the pixel size, and the acquired convoluted signal (d) is used to reconstruct the higher resolution intensity profile (e).

higher resolution intensity profile can be seen in Fig. 1e. It is evident that more information about the shape of the object can be extracted because of the sub-pixel shifting method without the disadvantages of reducing the detector element size or magnification, as described above. However, it does require an image scanning system and a longer acquisition time.

A push-broom HSI (Pb-HSI) system is used in our laboratory for plasma optical emission spectroscopy (OES) because of its fast acquisition and high light throughput.[21-24] Pb-HSI is a line scanning system which allows collecting information of one spatial dimension (y) and the spectral (λ) dimension simultaneously, while scanning the other spatial dimension (x) to complete the hyperspectral datacube. The spatial resolution in Pb-HSI system is still limited by the sampling distance, in this case, scan step/camera pixel size, mentioned above. Due to the scanning nature, however, the Pb-HSI is especially well suited for SPS. In addition, typical shortcomings of magnification approaches can be avoided, particularly a smaller FOV, which is significantly important given our plasma sources of interest require a larger FOV in the height dimension (y) vs. the width dimension (x).

In this study, we present the implementation of sub-pixel shifting on a Pb-HSI system. Also, the effects of noise content in the acquired raw images on the resulting SPS deconvolution is characterized. The designed models allow for the error characterization of the SPS algorithm implemented with different levels of white Gaussian noise to be reported for the first time. Several noise filtering schemes are compared and optimized based on the images of a resolution target. In addition, geometric super-resolved plasma OES images obtained via SPS Pb-HIS are reported for the first time. The optimized SPS method will be applied in a future study for extracting radially resolved plasma OES maps from line-of-sight images, to obtain higher

resolution and an increased number of data points for better performance from Abel's inversion fitting protocols along the dimension of interest.

Experimental

The push-broom hyperspectral imaging system

The PBHSI system here is described by Kroschk *et al* [21]. In short, the light collection optics include collimating and focusing triplet lenses (CaF2/fused silica/CaF2, 100 mm nominal focal length, Bernhard-Halle GmBH, Germany), and a 90-degree turning plane mirror in between. The mirror and focusing lens are mounted on a linear motorized stage (MTS50-Z8, Thorlabs Ltd., UK), allowing the scan of the image across the entrance slit of the spectrograph (x-dimension). The motorized stage has a bidirectional repeatability of 1.6 µm in a 50 mm travel range, therefore, the minimum scan step here was set to 2 µm. The spatial resolution of the PB-HSI system was characterized at 560 nm center wavelength with a USAF 1951 negative target (R3L3S1N, Thorlabs Ltd. UK) and a white LED table lamp light source passed through two consecutive ground glass diffusers (DG100X100-220 and DG100X100-600, Thorlabs Ltd., UK) to improve the field homogeneity.

The spectrograph (IsoPlane SCT 320, Princeton Instruments, USA) has a 327 mm focal length with a 300 g/mm grating (9.77 nm/mm linear dispersion and f/4.6 aperture ratio). The entrance slit has a maximum height of 13 mm and a minimum width of 10 µm. An ICCD camera (iStar 334T, Thorlabs Ltd., UK) with 1024 × 1024 pixels, 13 × 13 µm pixel size, was operated in the gain range from 750 to 2750, with 15 on-chip accumulations and 0.1s gate duration. A homemade LabVIEW program previously described[21] was used for automated acquisition and the corresponding hyperspectral datacubes were reoriented and displayed in ImageJ.[25] The

motorized stage was moved in a stepwise mode, as opposed to continuously, such that the stage was stationary during the ICCD spectral acquisition at each adjacent motor position. The slit width (pixel size) was set to 10 µm. The motorized stage scan step (x-dimension) was set to 10 µm for regular imaging, or 2 µm for sub-pixel shifting measurements.

Sub-pixel shifting

The theory of sub-pixel shifting is described by Pernechele and Yang *et al* [19, 20]. Essentially, when performing regular imaging with a discrete array detector, i.e. an ICCD camera, the resolution is in great part limited by the sampling distance. Assuming that the **true** signal intensity profile along a certain spatial axis (i.e. x dimension) is represented by a function $f(x)$. The **detected** signal intensity can then be expressed by:

$$F_R(n) = \int_{nd}^{(n+1)d} f(x)\,dx, \qquad n = 0,1,...,N-1 \tag{1}$$

Where d represents the sampling distance, n corresponds to the pixel number, and N is the total number of pixels. $F_R(n)$ represents the intensity of the signal acquired at the (n+1)th pixel. In an array detector, the sampling distance, or distance between the center of adjacent detector elements, defines the pixel size of the detected image, thus limiting the spatial resolution (Fig. 1a and 1c). The sub-pixel shifting method introduces a fixed smaller (sub-pixel) sampling distance as p=d/K, where K is the SPS coefficient (integer), i.e. the number of sub-pixel steps (Fig. 1b). Thus,

$$F_{SPS}(n_k) = \int_{nd+kp}^{(n+1)d+kp} f(x)dx, \qquad k = 0,1,...,K-1,\ n = 0,1,...,N-1 \tag{2}$$

where $F_{SPS}(n_k)$ is the detected signal at the (n+1)th pixel of the kth acquisition. The sub-pixel shifted acquisition increases the sampling rate by K times, thus the spatial resolution will be improved if

$F_{SPS}(n_k)$ is used for reconstructing the true image. The improved resolution should be equivalent to having an ideal array detector with a smaller pixel size d/K with a detected intensity function:

$$F_i(m) = \int_{md/K}^{(m+1)d/K} f(x)dx, \qquad m = 0,1,...,K-1 \tag{3}$$

Where m is the number of the smaller pixel, thus m = nK. However, a single sub-pixel shifted image is still the result of the convolution of K sub-pixel images (Fig. 1d). To calculate the deconvoluted signal equivalent to $F_i(m)$ from the actual acquired sub-pixel shifted signal $F_{SPS}(n)$, equation (2) and (3) can be rewritten as:

$$F_{SPS}(n) = \sum_{m=nK+k}^{(n+1)K-1+k} F_i(m), \qquad k = 0,1,...,K-1,\ \ n = 0,1,...,N-1 \tag{4}$$

Then, the relationship between $F_{SPS}(n_k)$ and $F_i(m)$ can be expanded as:

$$F_i(m+K) = F_{SPS}(m+1) - F_{SPS}(m) + F_i(m) \tag{5}$$

In the case where the first K values of sub-pixel shifted data (equivalent to $F_i(0), F_i(1), ..., F_i(K-1)$) are known, the whole sub-pixel shifted image $F_{SPS}(n_k)$ can be deconvoluted into the higher resolution image $F_i(m)$ (Fig. 1e).

Sub-pixel shifting algorithm performance characterization

The deconvolution efficiency, resolution improvement, and error robustness of the SPS algorithm were characterized using model data of a resolution target intensity profile and a representative plasma optical emission intensity profile created in MATLAB (R2017a, The Math Works, Inc., USA). All modelling and data analysis was performed on a computer with a Windows system (Windows 10 Pro, 64-bit operating system; Inter(R) Core(TM) i5-3230M CPU@2.60GHz processor and 16 GB RAM).The noise-free target intensity profile shape is representative of the cross-section of the USAF 1951 negative resolution target. The background intensity was set to 0

and signal intensities were set to 900 and 6000, to simulate the dark-field background and the bright field of target lines measured with the Pb-HSI system. The line pair width was adjusted to represent target elements with line frequencies ranging from group 2/element 1 (4 line-pairs/mm) to group 6/element 6 (114 line-pairs/mm).

The representative model plasma optical emission data was chosen to reflect a line-of-sight integrated profile with a lower intensity at the axial position, as observed in many plasma OES images:[26]

$$f(x) = \frac{8}{105}(\sqrt{1-x^2})(19+34x^2-125x^4+72x^6), \qquad for\ 0 \le x \le N \tag{6}$$

where N is the total number of data points across the profile, and x is the datapoint index.

Simulation of regular imaging (Eq. 1, slit width/pixel size = 10 μm, scan step/sampling distance = 10 μm) and sub-pixel shifted imaging (Eq. 2, slit width/pixel size = 10 μm, scan step/sampling distance = 2 μm) was performed with model data along the x dimension, 1 data point every 1 μm. Thus, 10 data points of the simulated "true" image profile were integrated into one pixel in accordance with the given slit width/pixel size of 10 μm. Sub-pixel shifted image deconvolution was achieved by using K=5, according to the sampling distance (p = d/K, 2 μm = 10 μm/5) and Eq. 5.

Error characterization and noise filtering

The noise in the images acquired with the Pb-HSI system was characterized by calculating the standard deviation of three images taken with the same plasma operation conditions. Noise was added into the model intensity profiles to better simulate the images taken with the push-broom HSI system. The added noise follows a Gaussian (normal) distribution and is produced with a random number generator function in MATLAB. The noise was first added to the

simulated signal after the slit width/pixel size convolution, and its amplitude was varied from 0.45% to 27% relative standard deviation (RSD). The SPS deconvolution was then performed on the noisy-profiles and its residual with respect to the noise-free original signal was calculated. In addition, noise power spectra were obtained from simulated SPS intensity profiles vs those acquired with the PB-HSI system. The noise in the SPS deconvoluted model images was minimized with an optimized lowpass filter and its performance was compared with an optimized notch filter. The optimized noise filter was then used in the reconstruction of the experimentally obtained SPS Pb-HSI images.

Atmospheric pressure dielectric barrier discharge

The optimized SPS Pb-HSI protocol was used for acquiring plasma OES images from a micro-size dielectric barrier discharge (µDBD). Helium gas with a purity of 99.999% was used for discharge gas (Ultra High Purity 5.0 Grade Helium, Airgas, USA) and the flow rate was set to 0.400 slpm. An applied AC voltage of 6-8 kV at 30 kHz (PVM500, Information Unlimited, USA) was used to generate the discharge in a fused silica capillary (150 µm i.d. and 360 µm o.d., Polymicro Technologies, USA). The aluminum foil ring electrodes were placed co-axially outside of the capillary separated by 5 mm. The power electrode was placed 5 mm away from the capillary tip, which was set 1 mm away from the copper block sample surface.

Results and discussion

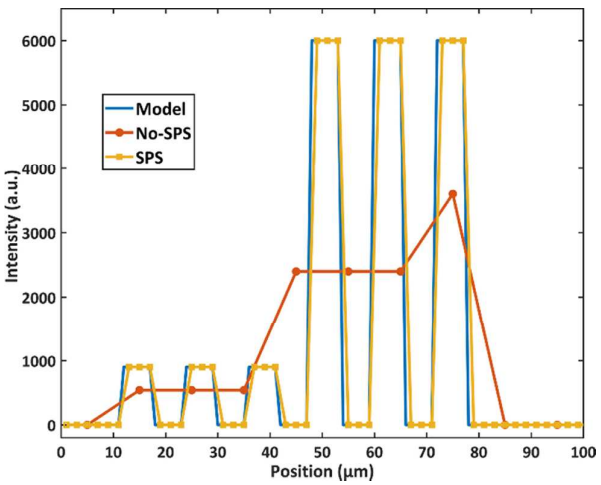

Fig.2 Model intensity profile (blue) with a data point every 1 µm. The typical imaging, with a sampling rate every 10 µm, cannot resolve the features (red). The SPS imaging protocol, with a sampling rate every 2 µm, can clearly resolve the original model data features (yellow).

SPS of noise-free resolution target model data

A model intensity profile that simulates intensity changes across an element of a 1951 USAF target (six 6 µm-wide square peaks separated by 6 µm) was first used to assess the performance of the sub-pixel shifting algorithm. Figure 2 shows the original model data, with 1 data point every µm, and the resulting profiles when sampled with a pixel size of 10 µm, to simulate the Pb-HSI system's slit width. When typical imaging/sampling is used (w/o SPS), i.e. one sample every 10 µm, it is evident that the features cannot be resolved. On the other hand, the SPS imaging protocol, i.e. one sample every 2 µm, allows resolving the features of the original model data, even when the pixel size is 10 µm. These results can be understood in terms of the Shannon-Nyquist theorem, where the sampling rate must be more than twice as high as the frequency of the signal of interest to maintain fidelity. Furthermore, it shows the SPS algorithm is accurate.

SPS Pb-HSI plasma OES image

The next step was to implement the SPS imaging experimentally on the Pb-HSI system. For this purpose, the optical emission images of an atmospheric pressure µ-DBD were obtained. Figure 3a shows the raw SPS µ-DBD image, with 10 µm spectrograph slit width and 2 µm scanning step size, of the N_2^+ emission at 391 nm (note the different scales for x and y-axis). Upon deconvolution (Fig. 3c), however, the SPS image shows an error

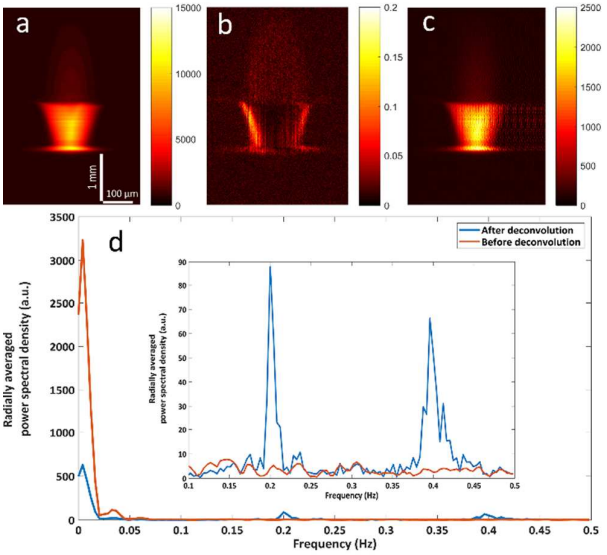

Fig.3 Raw/convoluted SPS Pb-HSI µDBD OES image of N_2^+ emission at 391 nm (a), its RSD map (b), and the same image after deconvolution (c). The radially averaged power spectrum (d) of the image before the deconvolution (red) and after the deconvolution (blue); insert figure is the zoom-in region from 0.1 Hz to 0.5 Hz.

which was not observed with the model data. The error seems to be periodic in nature and increases toward the right side of the image, which coincides with the Pb-HSI scanning direction. After applying a Fourier Transform (FT), the radially averaged power spectrum of the images before and after convolution (Fig. 3d) were compared. It is evident that the image after the deconvolution features 2 peaks at f1=0.2 Hz and f2=0.4 Hz. The periodic error seems to show an inverse dependence with the number of sub-pixel steps 1/K (SI section 1), and it only shows up when there is noise present in the raw SPS data before deconvolution, as confirmed by the noise-free model in Figure 2. This type of periodic error comes from the difference between sub-pixel information deconvoluted from the measured SPS image and the true value of the sub-pixel information with a period of K, and has been shown to appear at F, 2F, 3F…, where F=1/K. [20]

In order to better understand the noise effects, the RSD (Fig. 3b) was calculated from three consecutive raw SPS plasma OES images, taken under the same conditions as in Fig. 3a. The RSD of the background is below 2%, and the RSD of the signal ranges from 1% to 10% around the axial position and can rise as high as 18% at the edge of the plasma. These values are helpful to guide the characterization of the effects of noise in the raw SPS data on the deconvoluted profiles which was performed through the addition of varying levels of Gaussian noise to the model data.

For this purpose, varying content of Gaussian noise (RSD = 0.45% - 27%) was added to the model SPS intensity profiles, with a shape representative of plasma OES, and the resulting periodic noise in the deconvoluted profiles was characterized. A selected model SPS intensity profile plot with added 0.9% RSD, before and after deconvolution, and their corresponding power spectra are shown in Figure 4. The power spectra show that the signal appears at the low-

frequency region. In contrast, a clear pattern of periodic error emerges after the deconvolution, at frequencies of 0.2 Hz and 0.4 Hz. The deconvoluted model signal frequency content is very similar to the one obtained for the SPS Pb-HSI plasma OES in Figure 3, thus, it confirms the validity of this approach for studying the effects of noise.

Noise removal and filter optimization

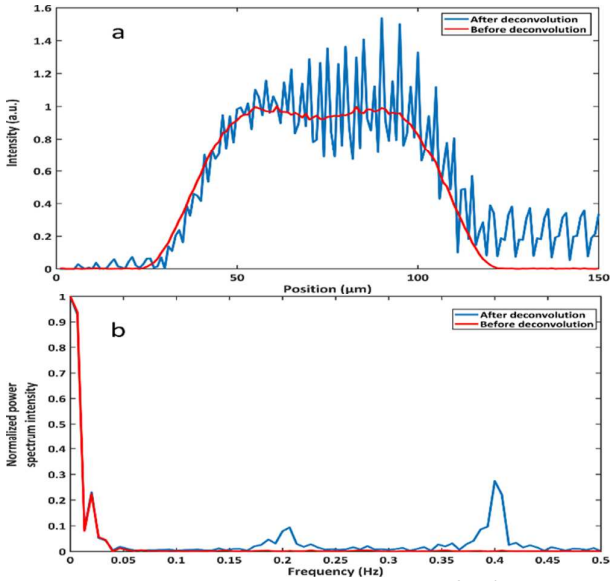

Fig.4 Model SPS plasma OES intensity profile (10 μm pixel width, 2 μm scan step) with 0.9% RSD noise added before and after deconvolution (a). The frequency of the periodic noise can be observed by comparing the corresponding power spectra (b).

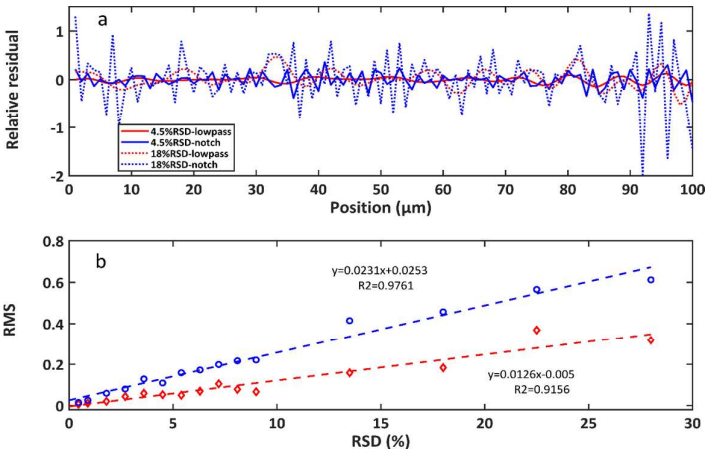

Fig. 5 Relative residual distribution across the deconvoluted model plasma profile after noise filtering is applied at two RSD levels (a). The RMS of the relative residual distribution as a function of increasing RSD after lowpass filter (circle) or notch filter (diamond) (b).

Knowledge of the periodic noise frequency allows optimized noise filtering. Here, a low-pass filter and a notch filter were implemented for minimizing the noise content in the deconvoluted SPS profiles. The optimized cut-off frequency of the low-pass filter was determined to be 0.15 Hz, when varied between 0.15 Hz and 0.2 Hz, while the optimized notch filter blocked frequencies were set between 0.15 Hz – 0.25 Hz and 0.35 Hz – 1 Hz with a Gaussian shape to prevent ringing effects (SI section 2). The relative residual across the signal profile after filtering was used to assess the noise filtering efficiency. The residual values are approximately evenly

distributed across the intensity profile (Fig. 5a), and it is evident that, for the selected 4.5% RSD and 18% RSD noise added, the low pass filter is more efficient at minimizing the noise content. In model prediction, the root-mean-square error (RMSE) is frequently used to evaluate the fidelity of the model by measuring the differences between the observed data and the predicted data.[27, 28] Thus, given the general shape of the residuals, the root mean square (RMS) residual across the profile, which is equivalent to RMSE, was used to evaluate the reconstruction noise filtering effectiveness at varying added RSD levels. Figure 5b shows the RMS has a linear relationship with the noise level, and that the lowpass filter results in more efficient minimization of the SPS deconvolution error. Thus, the lowpass filter was selected for the experimental SPS images obtained with the Pb-HSI system.

Spatial resolution improvement by SPS

SPS images of the 1951 USAF resolution target were obtained with the Pb-HSI to evaluate the spatial resolution improvement after noise filtering. Figure 6 shows group 5 elements 1-6 acquired by regular imaging (a, 10 µm slit width/pixel size, 10 µm scan step/sampling distance) and by the SPS protocol (b, 10 µm slit width/pixel size, 2 µm scan step/sampling distance) where it is evident upon inspection that the spatial resolution in the scanning (x-) dimension is enhanced by SPS. The peak-to-valley ratio (Fig. 6c) of the intensity profile across group 5/element 6 (57 line-pairs/mm or line width = 8.77 µm) in the SPS image is 1.9, while the peaks are not resolvable in the regular image. The improved resolution can also be observed in the peak-to-valley ratio of group 5/element 1 (32 line-pairs/mm or line width = 15.63 µm) which is 5.8 in the SPS image, while it is only 1.6 in the regular image. In fact, the regular image only shows a peak-to-valley ration of 5.8 for group 3/element 6 (not shown, 14.25 line-pairs/mm or

line width = 35.08 µm). The results confirm that the SPS method is a powerful tool for the spatial resolution improvement along the scanning direction in a Pb-HSI system. It is noteworthy to mention that 2D monochromatic images were first extracted from the collected hyperspectral data cubes and that the total ensuing processing time (deconvolution and noise filtering) of a 2D monochromatic image is less than 1s.

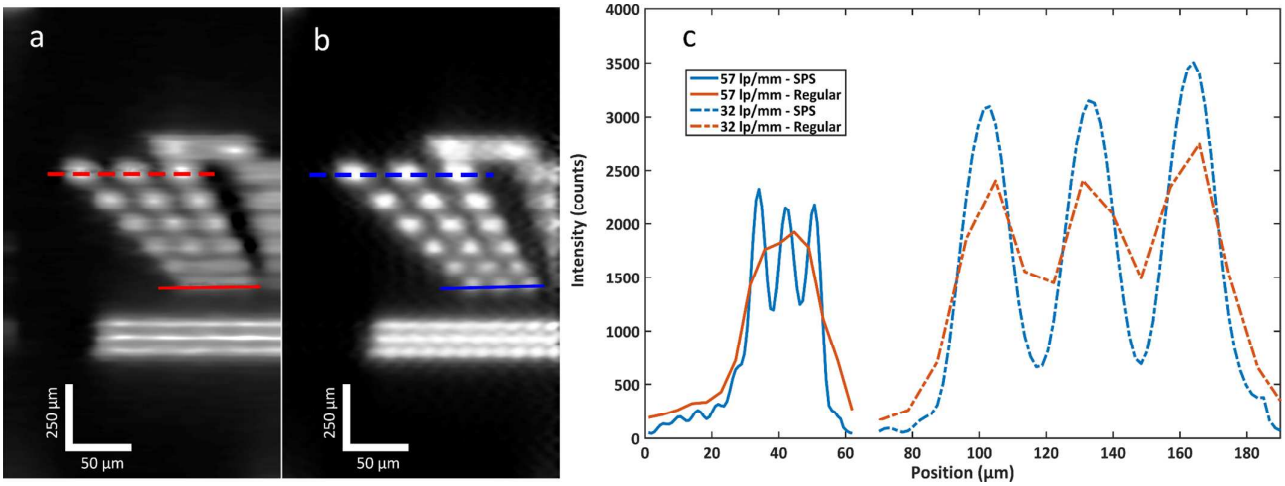

Fig. 6 Images of USAF resolution target group 5 acquired by a) regular imaging (10 µm pixel size/sampling distance), and b) SPS imaging (10 µm pixel size, 2 µm sampling distance). The corresponding group 5/ element 1 (dotted) and group 5/ element 6 (solid) intensity profiles are shown in c) for regular (red) and SPS imaging (blue).

Pb-HSI of plasma OES by the optimized SPS protocol

The optimized SPS protocol was implemented for the acquisition of Pb-HSI images of the optical emission from the atmospheric pressure µDBD with geometric super-resolution. The image at 706.5 nm shows the spatial distribution of He I ($3s\ ^3S_1$ - $2p\ ^3P_{0,1,2}^o$) excited species (Fig. 7a). The intensity is higher inside the capillary and decreases in the region between the end of the capillary and the sample surface, which indicates the excited He I transfers its energy to other species outside the capillary. The image at 391 nm shows the spatial distribution of the N_2^+ excited species, 0-0 first negative system B $^2\sum_u^+$ - X $^2\sum_g^+$ transition (Fig. 7b). It is evident that the

N_2^+ has a much higher intensity in the open-air region between the capillary and the sample surface, indicating the N_2^+ is formed where the plasma afterglow makes contact with the ambient air. This process may include the charge transfer mechanism with He^+ and He_2^+,[29] or the Penning ionization mechanism with the helium metastables.[30] In contrast, the image obtained at 337 nm (Fig. 7c), corresponding to the band head emission of N_2, 0-2 second positive system from C $^3\Pi_u$ - B $^3\Pi_g$ transition, shows an increasing intensity from the outlet of the capillary towards the sample surface where it reaches a maximum. This trend, together with the N_2^+ intensity distribution, indicates that the N_2 is formed by the electron recombination process with N_2^+.[31] Fig. 7d shows the atomic oxygen optical emission image obtained at 777.4 nm, from the ($^4S^o$)3p $^5P_{1,2,3}$ - ($^4S^o$)3p $^5S_2^o$ transition. The slightly higher intensity in the capillary compared to the N_2 image suggests that the atomic oxygen generated from the molecular oxygen in the open air may be diffusing into the capillary. However, further experiments are needed to confirm this observation.

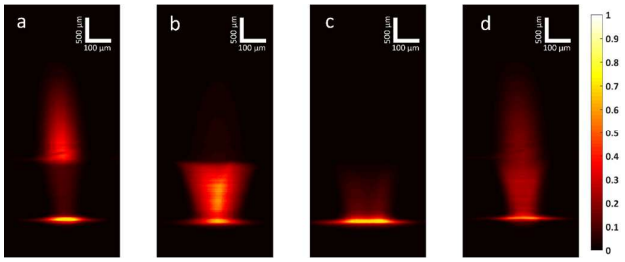

Fig. 7 SPS Pb-HSI images (10µm pixel size, 2µm scan step) after deconvolution and lowpass filter. a) He I emission at 706.5 nm; b) N2+ emission at 391 nm; c) N2 emission at 337 nm and d) O I emission at 777.4 nm. Notice the emission intensities are normalized to itself.

Of particular note is the lateral distribution of the N_2 optical emission, which shows a lower intensity at the axial position. However, the current images are integrated through the line-of-sight. Thus, it is evident that radially resolved images are needed to improve the understanding of the underlying mechanisms of plasma/ambient-air/sample interaction. The obtained images show a successful reconstruction performed by applying the SPS technique and a lowpass frequency filter. Compared with the regular images, the SPS images have a higher spatial resolution in x-

dimension while maintaining the FOV in y-dimension. Current work in our laboratory involves developing a 3D image reconstruction method based on an Abel's inversion protocol for extracting radially resolved information. The SPS Pb-HSI acquisition will not only allow higher resolution in the lateral dimension but also to obtain more data points which will greatly improve Abel's inversion fitting.[26]

Conclusions

The geometric super-resolution method based on sub-pixel shifting was successfully implemented along the scanning dimension on a Pb-HSI system. Periodic error in the SPS deconvoluted images was identified and traced to the noise present in the raw SPS images. Frequency noise filters were designed to help minimize the error, and the optimized lowpass filter proved to remove the noise more efficiently than the notch filter scheme. SPS Pb-HSI images of the 1951 USAF target confirmed that the improved resolution was achieved. It is evident that this method successfully improves the spatial resolution by allowing separation of the pixel size and the sampling rate. The advantage of the SPS protocol is that resolution improvement does not come with a decrease of FOV, loss of light throughput, or a shrink in the size of the detecting elements, which are typical of conventional approaches. These advantages allow Pb-HSI to be implemented for applications requiring higher spatial resolution. The proof-of-principle SPS Pb-HSI images of an atmospheric pressure μ-DBD plasma jet showed the applicability to gain further insights of OES plasma diagnostics with greatly improved spatial resolution. Current and future work involves exploring further error minimization approaches, such as the use of a lock-in amplifier or auto-correlation; a motorized stage with smaller scan step size (higher sampling frequency) to achieve higher spatial resolution; and implementing SPS in the λ-dimension to achieve higher spectral resolution.

Conflicts of interest

There are no conflicts to declare.

Acknowledgments

The authors gratefully acknowledge the financial support from the National Science Foundation under CHE – 1610849.

References

1. A. F. Goetz, G. Vane, J. E. Solomon and B. N. Rock, *Science*, 1985, **228**, 1147-1153.
2. E. Adam, O. Mutanga and D. Rugege, *Wetlands Ecology and Management*, 2010, **18**, 281-296.
3. M. Govender, K. Chetty and H. Bulcock, *Water SA*, 2007, **33**, 145-151.
4. H. Liang, *Applied Physics A: Materials Science and Processing*, 2012, **106**, 309-323.
5. L. M. Dale, A. Thewis, C. Boudry, I. Rotar, P. Dardenne, V. Baeten and J. A. F. Pierna, *Applied Spectroscopy Reviews*, 2013, **48**, 142-159.
6. X. Briottet, Y. Boucher, A. Dimmeler, A. Malaplate, A. Cini, M. Diani, H. Bekman, P. Schwering, T. Skauli, I. Kasen, I. Renhorn, L. Klasén, M. Gilmore and D. Oxford, 2006.
7. H. Xu and X. J. Wang, *Hongwai yu Jiguang Gongcheng/Infrared and Laser Engineering*, 2007, **36**, 13-17.
8. R. Padoan, A. G. Steemers, M. E. Klein, B. Aalderink and G. de Bruin, *QUANTITATIVE HYPERSPECTRAL IMAGING OF HISTORICAL DOCUMENTS: TECHNIQUE AND APPLICATIONS*, 2008.
9. R. L. Schuler, P. E. Kish and C. A. Plese, *Journal of Forensic Sciences*, 2012, **57**, 1562-1569.
10. J. Kuula, I. Pölönen, H. H. Puupponen, T. Selander, T. Reinikainen, T. Kalenius and H. Saari, *Proceedings of SPIE - The International Society for Optical Engineering*, 2012, **8359**.
11. R. Vejarano, R. Siche and W. Tesfaye, *International Journal of Food Properties*, 2017, DOI: 10.1080/10942912.2017.1338729, 1-34.
12. D. Wu and D.-W. Sun, *Innovative Food Science & Emerging Technologies*, 2013, **19**, 15-28.
13. D. Wu and D.-W. Sun, *Innovative Food Science & Emerging Technologies*, 2013, **19**, 1-14.
14. F. Masia, A. Glen, P. Stephens, P. Borri and W. Langbein, *Analytical Chemistry*, 2013, **85**, 10820-10828.
15. D. F. Barbin, G. ElMasry, D.-W. Sun and P. Allen, *Food Chemistry*, 2013, **138**, 1162-1171.
16. X. Xu, Y. Zhong, L. Zhang and H. Zhang, *IEEE Journal of Selected Topics in Applied Earth Observations and Remote Sensing*, 2013, **6**, 580-593.
17. J. Ojeda-Castaneda, S. Han, P. Jia, J. Fang, D. Fan, L. Qian, Y. Gu, X. Yan, H. Wang and D. Wen, presented in part at the Selected Papers from Conferences of the Photoelectronic Technology Committee of the Chinese Society of Astronautics: Optical Imaging, Remote Sensing, and Laser-Matter Interaction 2013, 2014.
18. B. Ning and X. Gao, *Neurocomputing*, 2013, **117**, 128-137.
19. H. D. Yang, K. X. Chen, Q. S. He and G. F. Jin, *Spectrosc Spect Anal*, 2009, **29**, 3169-3172.
20. C. Pernechele, L. Poletto, P. Nicolosi and G. Naletto, *Optical Engineering*, 1996, **35**, 1503-1510.
21. M. Kroschk, J. Usala, T. Addesso and G. Gamez, *Journal of Analytical Atomic Spectrometry*, 2016, **31**, 163-170.
22. C. Gonzalez de Vega, D. Alberts, V. Chawla, G. Mohanty, I. Utke, J. Michler, R. Pereiro, N. Bordel and G. Gamez, *Anal Bioanal Chem*, 2014, **406**, 7533-7538.
23. G. Gamez and K. Finch, *Spectrochimica Acta Part B: Atomic Spectroscopy*, 2018, **148**, 129-136.
24. G. Gamez, G. Mohanty and J. Michler, *Journal of Analytical Atomic Spectrometry*, 2014, **29**, 315-323.
25. C. A. Schneider, W. S. Rasband and K. W. Eliceiri, *Nat Methods*, 2012, **9**, 671-675.
26. G. C. Y. Chan and G. M. Hieftje, *Spectrochimica Acta Part B: Atomic Spectroscopy*, 2006, **61**, 31-41.
27. J. D. Usala, A. Maag, T. Nelis and G. Gamez, *Journal of Analytical Atomic Spectrometry*, 2016, **31**, 2198-2206.
28. R. J. Hyndman and A. B. Koehler, *International Journal of Forecasting*, 2006, **22**, 679-688.
29. G. C. Chan, J. T. Shelley, J. S. Wiley, C. Engelhard, A. U. Jackson, R. G. Cooks and G. M. Hieftje, *Anal Chem*, 2011, **83**, 3675-3686.
30. R. B. Cody, J. A. Laramée and H. D. Durst, *Analytical Chemistry*, 2005, **77**, 2297-2302.
31. G. C. Y. Chan, J. T. Shelley, A. U. Jackson, J. S. Wiley, C. Engelhard, R. G. Cooks and G. M. Hieftje, *Journal of Analytical Atomic Spectrometry*, 2011, **26**.